Fusion Engineering and Design 194 (2023) 113914

Contents lists available at ScienceDirect

Fusion Engineering and Design

journal homepage: www.elsevier.com/locate/fusengdes

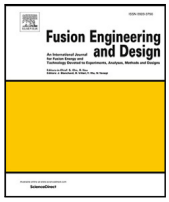

Nonlinear control of safety factor gradient in tokamaks using spatially variable electron cyclotron current drives

Sai Tej Paruchuri *, Eugenio Schuster

Mechanical Engineering and Engineering Mechanics, Lehigh University, Bethlehem, PA, USA

ARTICLE INFO

Keywords:
Safety factor gradient
Moving ECH&CD
Nonlinear control
Local safety factor control

ABSTRACT

Active control of plasma properties may be necessary to achieve stable operation of next-generation tokamaks over large time scales. Such control algorithms can regulate the plasma properties to avoid the onset of magnetohydrodynamic (MHD) instabilities. For instance, the global and local properties of the safety factor profile are linked to the onset of neoclassical tearing modes (NTMs). This work proposes a model-based control approach for deterring/delaying NTMs through active modulation of one of the safety factor properties - the gradient of the safety factor profile at a particular rational safety factor surface. In particular, a novel control-oriented model for the local safety factor gradient is developed. The nonlinear control model is governed by a nonautonomous ordinary differential equation that accounts for a given rational safety factor surface's spatial variation over time. To improve the controllability of the spatially evolving parameter, the control model treats ECH&CD positions, along with noninductive powers, as controllable variables. A nonlinear control algorithm based on feedback linearization with optimization is synthesized to achieve the objective of regulating the safety factor gradient around a given target. The proposed algorithm allocates optimal ECH&CD positions, in addition to auxiliary powers, at each time instant as the rational safety factor surface drifts to locations with a low control authority. Stability guarantees of the proposed control law are also discussed in this work. The proposed algorithm is tested for a DIII-D tokamak scenario in nonlinear simulations carried out using the Control Oriented Transport SIMulator (COTSIM). Both fixed and moving ECH&CD cases are studied, and their outcomes are compared. Simulation results demonstrate that enthusiastic regulation of the safety factor gradient can be achieved during the ramp-up and flat-top phases of tokamak operation in both fixed and moving ECH&CD cases. However, real-time updates of ECH&CD positions can prevent the saturation of auxiliary powers.

1. Introduction

Avoiding magnetohydrodynamic (MHD) instabilities like neoclassical tearing modes (NTMs), which can appear at locations with rational safety factor values and can disrupt plasma confinement, is critical for the success of next-generation tokamaks like ITER. One potential solution to prevent the onset of NTMs is to actively avoid certain low-order rational surfaces like $q = 1.5$ and $q = 2$. Control solutions exist in the literature that can be implemented on tokamaks to actively regulate the safety factor profile to avoid rational values. They can be broadly classified into global and local control algorithms. Global control algorithms actively regulate the whole safety factor profile. Some examples of such algorithms in the literature include robust control [1], linear quadratic optimal control [2,3], and model predictive control [4–6] control, infinite-dimensional Lyapunov-based control [7–9], passivity-based control [10], backstepping control [11], H_∞ control [12], feedback linearization [13,14]. By carefully selecting the target safety factor profiles which do not take low-order rational values, global control algorithms can be used to prevent the onset of NTMs. Local control algorithms are designed to regulate the safety factor values on a limited scale instead of the entire profile. In scenarios characterized by a monotonously increasing safety factor profile, the central safety factor control algorithm [15] can be used to maintain the safety factor value above a threshold rational value. In scenarios with reversed shear safety factor profile, the minimum safety factor control algorithm [16] can be used to achieve a similar effect.

In certain tokamak scenarios, rational safety factor values like $q = 1.5$ and $q = 2$ are impossible to avoid. Implementing the above-cited algorithms to shift the safety factor profile above the threshold rational values will only saturate the auxiliary drives. In such cases, simultaneously regulating the global and local shape of the safety factor profile

* Corresponding author.
E-mail address: saitejp@lehigh.edu (S.T. Paruchuri).

https://doi.org/10.1016/j.fusengdes.2023.113914
Received 27 April 2023; Received in revised form 3 July 2023; Accepted 5 July 2023
Available online 25 July 2023

may prevent/delay the onset of NTMs. A bulk of the above-cited global control algorithms can be implemented for varying the global shape of the safety factor profile. However, solutions for varying the local shape of the safety factor profile at the rational surfaces do not exist. The local shape of the safety factor profile can be varied by modifying the local gradient. However, such shaping is not straightforward since gradient regulation can pose three challenges: (i) conventional safety factor models do not capture gradient dynamics, (ii) conventional models do not account for rational surfaces' spatial drift, (iii) rational surfaces can move to locations where the auxiliary drive deposition is low. The first two challenges can be addressed by developing advanced models that govern the evolution of the slope at moving rational surfaces. On the other hand, since the target location is continuously drifting (possibly to locations with low auxiliary depositions), the controller could benefit from moving actuators.

This work develops a nonlinear safety factor gradient control algorithm that can regulate the local slope of the safety factor profile at any given rational surface. The contributions of this work are as follows. A control-oriented model for the safety factor gradient at a predefined rational surface is derived. The model is a one-dimensional ordinary differential equation. Conventionally, safety factor regulation is achieved using a model based on the poloidal flux gradient [14,16]. This is possible due to the direct relationship between the safety factor and the poloidal flux gradient. However, as discussed in Section 2 of this work, a model based on the poloidal flux gradient increases the complexity of the control problem. Hence, the model developed and used in this work is defined in terms of the safety factor's time derivative. The novel model treats neutral beam injector (NBI) and electron cyclotron heating & current drive (ECH&CD) powers as the actuators. In addition to the auxiliary drive powers, the position of the ECH&CDs is also considered a controllable variable. The effect of ECH&CD positions on the plasma dynamics is modeled using a shifting current deposition profile, initially introduced in [17] for regulating the minimum safety factor using moving ECH&CD. This work also develops a nonlinear control algorithm based on the "feedback-linearization with optimization" approach. Discussion on the stability of the controller is also presented in this work. The controller is tested for a DIII-D tokamak scenario using nonlinear simulations in the Control Oriented Transport SIMulator (COTSIM). Numerical analysis is carried out for both fixed and moving ECH&CD cases. Results demonstrate that the controller can track the target slope within the desired time frame. In addition, the simulation results also illustrate that controlling the ECH&CD positions can have added benefits in some scenarios.

This paper is organized as follows. Section 2 derives the model for safety factor gradient evolution around a rational surface. In Section 3, the model derived in Section 2 is used to synthesize a controller to track a target safety factor gradient. Section 4 examines the numerical simulation results carried out to test the controller performance in a DIII-D tokamak scenario. The conclusions and potential future extensions of this work are presented in Section 5.

2. Control-oriented safety factor gradient model

The objective of the section is to derive the control-oriented model for the safety factor gradient evolution. First, the general relation between the safety factor gradient and the poloidal flux gradient is analyzed. Then, a model for poloidal flux gradient, derived from the magnetic diffusion equation, is introduced. Next, a partial differential equation (PDE) for the evolution of the safety factor is derived using the relation between the safety factor and the poloidal flux gradient. Finally, approximations based on a finite difference scheme are introduced to simplify the PDE into an ordinary differential equation (ODE) for the safety factor gradient dynamics.

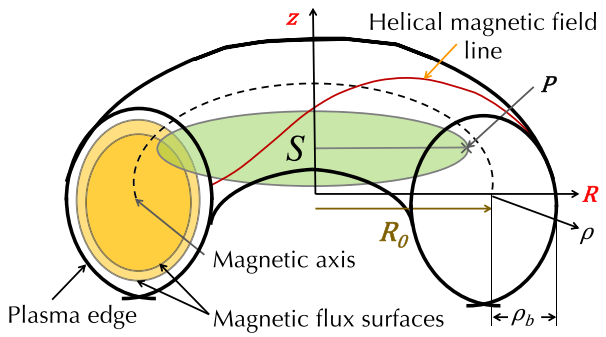

Fig. 1. An illustration of the magnetic field lines and nested flux surfaces in a tokamak.

2.1. Safety factor profile

The poloidal magnetic flux Ψ at a point P (shown in Fig. 1) in the tokamak is defined as $\Psi := \int_S \bar{B}_\theta \cdot d\bar{S}$, where $\bar{B}_\theta$ is the poloidal magnetic field and S denotes the surface enclosed by the toroidal loop passing through the point P and is perpendicular to the axis z that is shown in Fig. 1. As it will become evident in the following subsections and the analysis given in Appendix A, the plasma dynamics model used in this work is derived from the magnetic diffusion equation, which governs the evolution of the poloidal stream function ψ, a parameter related to the poloidal magnetic flux by the relation $\psi = \Psi/2\pi$. The points in the tokamak with a given value of poloidal magnetic flux or equivalently the poloidal stream function form what are commonly referred to as magnetic flux surfaces. Under ideal MHD conditions, important plasma properties like the safety factor and plasma pressure have a constant value on any given flux surface. Furthermore, the flux surfaces corresponding to different poloidal flux values form a nested collection of surfaces as shown in Fig. 1. Under the assumption of axisymmetry of the toroidal plasma, the dependence of the plasma properties like the safety factor can be reduced from three to two. Using the fact that the plasma properties of interest are constant on the nested flux surfaces, their spatial dependence can further be reduced to one. Such a simplification requires the definition of a spatial variable that indexes the nested flux surfaces. In this work, the normalized mean effective minor radius $\hat{\rho}$ is used as the spatial variable. It is defined as $\hat{\rho} := \frac{\rho}{\rho_b}$. In this equation, ρ is the mean effective minor radius and is given by $\rho := \sqrt{\frac{B_{\phi,0}\pi}{\Phi}}$, where the term $B_{\phi,0}$ refers to the magnitude of the toroidal magnetic field at the major radius R_0 of the tokamak and the term Φ refers to the toroidal magnetic flux. The term ρ_b is the value of mean effective minor radius ρ at the last closed magnetic flux surface.

The safety factor profile q is a plasma property that characterizes the pitch of the helical magnetic field in the tokamak. The value of the safety factor q at location $\hat{\rho}$ and time t is given by the mathematical expression

$$q(\hat{\rho},t) := -\frac{B_{\phi,0}\rho_b^2\hat{\rho}}{\theta(\hat{\rho},t)}. \tag{1}$$

In the above equation, the term $\theta := \frac{\partial\psi}{\partial\hat{\rho}}$ is the poloidal flux gradient. Due to the direct relation between q and θ, q-profile regulation can be achieved directly through controlling θ. For instance, control algorithms in [14,16,17] achieve the desired safety factor targets through regulation of θ. Such an indirect regulation is certainly possible for the problem of safety factor gradient control. However, it increases the complexity of the control problem. This becomes evident by taking the derivative of the safety factor given in (1) with respect to the spatial variable $\hat{\rho}$. The resulting equation takes the form

$$q'(\hat{\rho},t) := -\frac{B_{\phi,0}\rho_b^2}{\theta(\hat{\rho},t)} + \frac{B_{\phi,0}\rho_b^2\hat{\rho}}{(\theta(\hat{\rho},t))^2}\theta'(\hat{\rho},t). \tag{2}$$

In the above equation and in the subsequent sections, the notation $(\cdot)'$ denotes the first derivative with respect to the spatial variable $\hat{\rho}$. It is evident from the above equation that tracking a desired q' requires simultaneous control of two variables, θ and θ'. In certain scenarios, the poloidal flux gradient θ may achieve a steady-state value during the flat-top phase of the discharge. In such cases, the desired value of q' can be achieved by controlling only θ'. However, this limits the applicability of the controller in a broad class of scenarios. On the other hand, a model that defines the evolution of the safety factor will lead to a simpler control design. Such a model can be derived by taking the time derivative of the safety factor defined in (1). The resulting equations looks like

$$\dot{q}(\hat{\rho},t) = \frac{B_{\phi,0}\rho_b^2\hat{\rho}}{\theta(\hat{\rho},t)^2}\dot{\theta}(\hat{\rho},t) = -\frac{q(\hat{\rho},t)\dot{\theta}(\hat{\rho},t)}{\theta(\hat{\rho},t)}. \tag{3}$$

The notation $\dot{(\cdot)}$ denotes the derivative with respect to time. The above equation defines the evolution of q and not q'. However, the analysis presented in Section 2.3 will demonstrate that a gradient model can be derived from the above equation after introducing certain approximations.

2.2. Safety factor profile evolution model

The term $\dot{\theta}$ in (3) is governed by the PDE

$$\dot{\theta} = \left(h_{\eta,1}\theta'' + h_{\eta,2}\theta' + h_{\eta,3}\theta\right)u_\eta + \sum_{i=1}^{n_{nb}} h_{nb,i}u_{nb,i} + \sum_{j=1}^{n_{ec}} h_{ec,j}(\rho_{ec,j})u_{ec,j} + \left(h_{bs,1}\frac{1}{\theta} - h_{bs,2}\frac{\theta'}{\theta^2}\right)u_{bs}, \tag{4}$$

subject to the boundary conditions

$$\theta(0,t) = 0, \qquad \theta(1,t) = -k_{I_p}I_p. \tag{5}$$

The derivation of the above partial differential equation and the explicit definition of the individual terms appearing in it are presented in Appendices A and B. The terms $h_{(\cdot)}$ in (4) are functions of the spatial variable $\hat{\rho}$. On the other hand, $u_{(\cdot)}$ are the virtual inputs and functions of time t. The above model assumes there are n_{nb} NBIs and n_{ec} ECH&CD available for gradient control. Note that the above model also treats the ECH&CD position $\rho_{ec,j}$ corresponding to the jth ECH&CD as a controllable variable. Substituting (4) for $\dot{\theta}$ in (3) results in the PDE of the form

$$\dot{q} = -\frac{q}{\theta}\left[\left(h_{\eta,1}\theta'' + h_{\eta,2}\theta' + h_{\eta,3}\theta\right)u_\eta + \sum_{i=1}^{n_{nb}} h_{nb,i}u_{nb,i} + \sum_{j=1}^{n_{ec}} h_{ec,j}(\rho_{ec,j})u_{ec,j} + \left(h_{bs,1}\frac{1}{\theta} - h_{bs,2}\frac{\theta'}{\theta^2}\right)u_{bs}\right] \tag{6}$$

subject to the boundary conditions

$$q(0,t) = 0, \qquad q(1,t) = \frac{B_{\phi,0}\rho_b^2\hat{\rho}}{k_{I_p}I_p}. \tag{7}$$

Suppose $h^*_{nb,i}$ and $h^*_{ec,j}$ are defined such that

$$h^{*,min}_{nb,i} := h^{min}_{nb,i} \times (I_p^\gamma P_{tot}^\epsilon \bar{n}_e^\zeta)^{(-3/2+\zeta_{nb})}\bar{n}_e^{-1}, \tag{8}$$

$$h^{*,min}_{ec,j}(\rho_{ec,j}) := h^{min}_{ec,j}(\rho_{ec,j}) \times (I_p^\gamma P_{tot}^\epsilon \bar{n}_e^\zeta)^{(-3/2+\zeta_{ec})}\bar{n}_e^{-1}. \tag{9}$$

From (8) and (9), it is evident that the equations $h_{nb,i}u_{nb,i} = h^*_{nb,i}P_{nb,i}$ and $h_{ec,j}(\rho_{ec,j})u_{ec,j} = h^*_{ec,j}(\rho_{ec,j})P_{ec,j}$ hold. Substituting these equations into (6) results in a PDE in which the virtual inputs terms are replaced by the physical inputs, which are the NBI and EC powers in this case. The new PDE takes the form

$$\dot{q} = -\left(h_{\eta,1}\frac{\theta''}{\theta} + h_{\eta,2}\frac{\theta'}{\theta} + h_{\eta,3}\right)qu_\eta - \sum_{i=1}^{n_{nb}} \underbrace{\frac{h^*_{nb,i}}{\theta}q}_{g^*_{nb,i}} P_{nb,i}$$

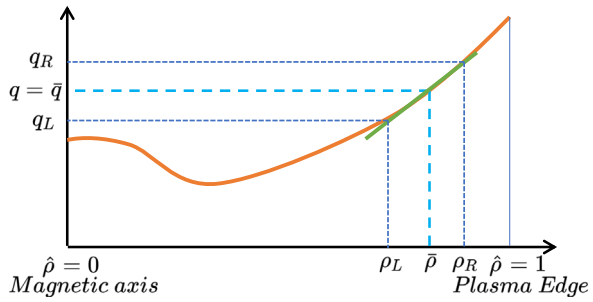

Fig. 2. Safety factor profile: central difference approximation of safety factor gradient at a rational surface $\bar{\rho}$.

$$- \sum_{j=1}^{n_{ec}} \underbrace{\frac{h^*_{ec,j}(\rho_{ec,j})}{\theta}q}_{g^*_{ec,j}(\rho_{ec,j})} P_{ec,j} - \frac{h_{bs,1}}{\theta^2}qu_{bs} - \frac{h_{bs,2}\theta'}{\theta^3}qu_{bs}. \tag{10}$$

2.3. Gradient approximation

The controller's goal is to track a target safety factor gradient q' at a rational safety factor surface $\bar{q}$, whose position is given by the function $\bar{\rho} : t \mapsto \bar{\rho}(t)$. Since real-time reconstruction techniques [18] can be used to obtain the safety factor profile during tokamak operation, the location of the rational surface $\bar{\rho}$ and the corresponding safety factor value is assumed to be known in this work. To simplify the control design, the gradient q' is approximated using the central difference scheme as

$$q'(\bar{\rho}) \approx \frac{q(\bar{\rho}+h) - q(\bar{\rho}-h)}{2h}, \tag{11}$$

where h is a constant. Fig. 2 gives an intuitive illustration of this approximation. Thus control of the gradient q' can be achieved by controlling the difference $q(\bar{\rho}+h)-q(\bar{\rho}-h)$. Note that this approximation is valid only in regions where the safety factor profile can be locally approximated as a straight line. Define the left control point ρ_L and corresponding safety factor q_L as

$$\rho_L := \bar{\rho}(\cdot) - h, \tag{12}$$

$$q_L := q(\rho_L(\cdot),\cdot). \tag{13}$$

The values of poloidal flux gradient and its first and second derivatives at the left control point are given by

$$\theta_L := \theta(\rho_L(\cdot),\cdot), \tag{14}$$

$$\theta'_L := \theta'(\rho_L(\cdot),\cdot), \tag{15}$$

$$\theta''_L := \theta''(\rho_L(\cdot),\cdot). \tag{16}$$

The values of the spatial functions in (10) at the location of the left control point are given by

$$h^L_{(\_)} := h_{(\_)} \circ \rho_L, \tag{17}$$

$$g^{*,L}_{nb,i} := g^*_{nb,i}(\rho_L(\cdot),\cdot), \tag{18}$$

$$g^{*,L}_{ec,j}(\rho_{ec,j}) := g^*_{ec,j}(\rho_{ec,j},\rho_L(\cdot),\cdot). \tag{19}$$

Evaluating the expression for $\dot{q}$ at $\hat{\rho} = \rho_L$ and using the above definitions results in the evolution equation

$$\dot{q}_L = -\left(h^L_{\eta,1}\frac{\theta''_L}{\theta_L} + h^L_{\eta,2}\frac{\theta'_L}{\theta_L} + h^L_{\eta,3}\right)q_Lu_\eta - \sum_{i=1}^{n_{nb}} g^{*,L}_{nb,i}P_{nb,i} - \sum_{j=1}^{n_{ec}} g^{*,L}_{ec,j}(\rho_{ec,j})P_{ec,j} - \frac{h^L_{bs,1}}{\theta^2_L}q_Lu_{bs} - \frac{h^L_{bs,2}\theta'_L}{\theta^3_L}q_Lu_{bs}. \tag{20}$$

The above equation can be written as

$$\dot{q}_L = \boldsymbol{g}_L(\boldsymbol{\rho}_{ec})^T\hat{\boldsymbol{u}} + \hat{c}_L, \tag{21}$$

where

$$\boldsymbol{g}_L(\boldsymbol{\rho}_{ec}) = \left[-g^{*,L}_{nb,1}, \dots, -g^{*,L}_{nb,n_{nb}}, -g^{*,L}_{ec,1}(\rho_{ec,1}), \dots, -g^{*,L}_{ec,n_{ec}}(\rho_{ec,n_{ec}})\right]^T,$$

$$\hat{\boldsymbol{u}} = \left[P_{nb,1}, \dots, P_{nb,n_{nb}}, P_{ec,1}, \dots, P_{ec,n_{ec}}\right]^T,$$

$$\hat{c}_L = -\left(h^L_{\eta,1}\frac{\theta''_L}{\theta_L} + h^L_{\eta,2}\frac{\theta'_L}{\theta_L} + h^L_{\eta,3}\right) q_L u_\eta - \frac{h^L_{bs,1}}{\theta^2_L} q_L u_{bs} - \frac{h^L_{bs,2}\theta'_L}{\theta^3_L} q_L u_{bs}.$$

Similarly, set $\rho_R = \bar{\rho}(\cdot) + h$ and define q_R, θ_R, θ'_R, θ''_R, $h^R_{(\_)}$, $g^{*,R}_{nb,i}$ and $g^{*,R}_{ec,j}$. Now, the evolution of q_R can be defined similar to the approach used above. Now, the control-oriented model for safety factor gradient is represented by the ordinary differential equation

$$\dot{q}_D = \dot{q}_R - \dot{q}_L = \underbrace{\left(\boldsymbol{g}_R(\boldsymbol{\rho}_{ec})^T - \boldsymbol{g}_L(\boldsymbol{\rho}_{ec})^T\right)}_{\boldsymbol{g}_D(\boldsymbol{\rho}_{ec})^T}\hat{\boldsymbol{u}} + \underbrace{\hat{c}_R - \hat{c}_L}_{\hat{c}_D}, \tag{22}$$

where $q_D := q_R - q_L$.

2.4. Error equations

Suppose the input $\hat{\boldsymbol{u}}$ has both feedforward $\boldsymbol{u}_{ff}$ and feedback $\boldsymbol{u}_{fb}$ components such that $\hat{\boldsymbol{u}} = \boldsymbol{u}_{ff} + \boldsymbol{u}_{fb}$. Furthermore, suppose that the goal of the controller is to track $\bar{q}_D$. Define c_D as $\check{c}_D(\boldsymbol{\rho}_{ec}) := \hat{c}_D + \boldsymbol{g}_D(\boldsymbol{\rho}_{ec})^T\boldsymbol{u}_{ff} - \dot{\bar{q}}_D$. Then, the governing equation of the error system is given by

$$\dot{\tilde{q}}_D = \dot{q}_D - \dot{\bar{q}}_D = \boldsymbol{g}_D(\boldsymbol{\rho}_{ec})^T\boldsymbol{u}_{fb} + \check{c}_D(\boldsymbol{\rho}_{ec}). \tag{23}$$

Thus, the goal of the controller is to stabilize the system governed by the above equation.

3. Nonlinear gradient control synthesis

The control model developed in the previous section is used to synthesize a nonlinear controller. First, the feedback linearization controller approach for the problem of interest is discussed. Then, real-time optimization problem necessary to implement the feedback linearization controller is formulated and solved.

3.1. Feedback linearization

The feedback linearization approach works on the principle of canceling the nonlinearities in the error equation [19,20]. Such cancellation allows the implementation of a linear controller on the resulting linear model. This control algorithm is advantageous in cases where the dynamics are not governed by a "structured" equation.

The goal of feedback linearization is to choose the feedback inputs $\boldsymbol{u}_{fb}$ such that the closed-loop equation takes the form

$$\dot{\tilde{q}}_D = -k_p\tilde{q}_D - k_I\int_0^t \tilde{q}_D, \tag{24}$$

where k_p and k_I are the proportional and integral gains. The stability of this closed-loop system is studied in Appendix C. This is achieved when the inputs $\boldsymbol{u}_{fb}$ satisfy the constraint

$$\boldsymbol{g}_D(\boldsymbol{\rho}_{ec})^T\boldsymbol{u}_{fb} + \underbrace{\check{c}_D(\boldsymbol{\rho}_{ec}) + k_p\tilde{q}_D + k_I\int_0^t \tilde{q}_D}_{c_D(\boldsymbol{\rho}_{ec})} = 0. \tag{25}$$

Substituting the above equation into (23) results in the linear equation given in (24). Thus, at each time t, choosing the input vector $\boldsymbol{u}_{fb}$ such that the algebraic constraint given in (25) is satisfied results in the linear closed-loop system. Since the closed-loop system is asymptotically stable (refer to Appendix C), the error will eventually converge to zero. Note that there are $n_{nb} + n_{ec}$ powers available for control. On the other hand, the dynamics and the control algorithm impose only two algebraic constraints (25) and (A.5). Note that (A.5) must be satisfied since P_{tot} is assumed to be prescribed and the total sum of the noninductive powers must equal the prescribed value. Thus, in scenarios where $n_{nb} + n_{ec} > 2$ multiple combinations of the auxiliary actuator powers can satisfy the two algebraic constraints. Optimization is used to select a unique set inputs. Another major advantage of implementing optimization is that, as presented in the next section, it can be adapted to incorporate ECH&CD positions $\boldsymbol{\rho}_{ec} := [\rho_{ec,1}, \dots, \rho_{ec,n_{ec}}]^T$ as controllable variables in addition to the auxiliary powers.

3.2. Optimization problem

The optimization problem is formulated as follows: At each time t,

$$\arg\min_{\boldsymbol{u}_{fb},\boldsymbol{\rho}_{ec}} f(\boldsymbol{u}_{fb}) = \arg\min_{\boldsymbol{u}_{fb},\boldsymbol{\rho}_{ec}} \boldsymbol{u}^T_{fb}Q\boldsymbol{u}_{fb}, \tag{26}$$

subject to the algebraic constraints

$$g_1(\boldsymbol{u}_{fb},\boldsymbol{\rho}_{ec}) = \boldsymbol{g}_D(\boldsymbol{\rho}_{ec})^T\boldsymbol{u}_{fb} + c_D(\boldsymbol{\rho}_{ec}) = 0, \tag{27}$$

$$g_2(\boldsymbol{u}_{fb}) = \mathbf{1}^T\boldsymbol{u}_{fb} + c_p = 0, \tag{28}$$

where $c_p = -P_{tot,fb}$, and $\mathbf{1} = [1, \dots, 1]^T \in \mathbb{R}^{n_{nb}+n_{ec}}$. The term $Q \in \mathbb{R}^{(n_{nb}+n_{ec})\times(n_{nb}+n_{ec})}$ is a diagonal matrix that weighs the different noninductive powers. The control algorithm presented in this work differs from the conventional optimal and predictive control algorithms in that the above finite-dimensional optimization problem is solved as each time t in real-time. On the other hand, optimal and predictive control algorithm solve an infinite-dimensional problem over a time window of finite or infinite width. In the above formulation, note that the ECH&CD positions do not explicitly appear in the cost function and affect only one of the algebraic constraints. However, treating them as controllable variables makes the algebraic constraint nonlinear. Such a problem can be solved using nonlinear programming methods [21]. However, such a computation can be computationally expensive for real-time implementation. For practical implementation of the controller presented in this work, the optimization problem is first solved by treating the EC positions as constants rather than controllable variables. Then, an iterative procedure is implemented to determine the optimal combination of auxiliary powers and EC positions.

3.2.1. Fixed EC position

Suppose that the EC positions are fixed at $\bar{\boldsymbol{\rho}}_{ec} := [\bar{\rho}_{ec,1}, \dots, \bar{\rho}_{ec,n_{ec}}]^T$. Define $\boldsymbol{g}^*_D(t) := \boldsymbol{g}_D(\bar{\boldsymbol{\rho}}_{ec}, t)$. The algebraic constraint given in (27) simplifies to a linear equation of the form

$$g^*_1(\boldsymbol{u}_{fb}) = \boldsymbol{g}^{*\,T}_D\boldsymbol{u}_{fb} + c^*_D = 0, \tag{29}$$

where $c^*_D(t) := c_D(\bar{\boldsymbol{\rho}}_{ec}, t)$. At time t, the optimal feedback inputs $\boldsymbol{u}^*_{fb}$ that minimize the cost function defined in (26) such that (27) and (28) are satisfied is given by

$$\boldsymbol{u}^*_{fb} = \frac{1}{2}Q^{-1}\begin{bmatrix}\boldsymbol{g}^*_D & \mathbf{1}\end{bmatrix}A^{-1}\boldsymbol{c}, \tag{30}$$

where

$$A = \begin{bmatrix}\boldsymbol{g}^{*\,T}_D Q^{-1}\boldsymbol{g}^*_D & \boldsymbol{g}^{*\,T}_D Q^{-1}\mathbf{1} \\ \mathbf{1}Q^{-1}\boldsymbol{g}^*_D & \mathbf{1}Q^{-1}\mathbf{1}\end{bmatrix}, \qquad \boldsymbol{c} = \begin{bmatrix}-2c^*_D \\ -2c_p\end{bmatrix}. \tag{31}$$

The detailed steps involved the derivation of the closed-form expression of the optimal input are given in Appendix D.

3.2.2. Incorporation of EC positions into control algorithm

To treat the EC positions as controllable variables, a finite, discrete set $\Omega \subset \mathbb{R}^{n_{ec}}$ of possible EC positions is considered. Each element of the set is a vector in $\mathbb{R}^{n_{ec}}$ of the form $[\rho_{ec,1}, \dots, \rho_{ec,n_{ec}}]^T$. The optimal set of EC positions and the corresponding auxiliary powers are computed using the following iterative approach.

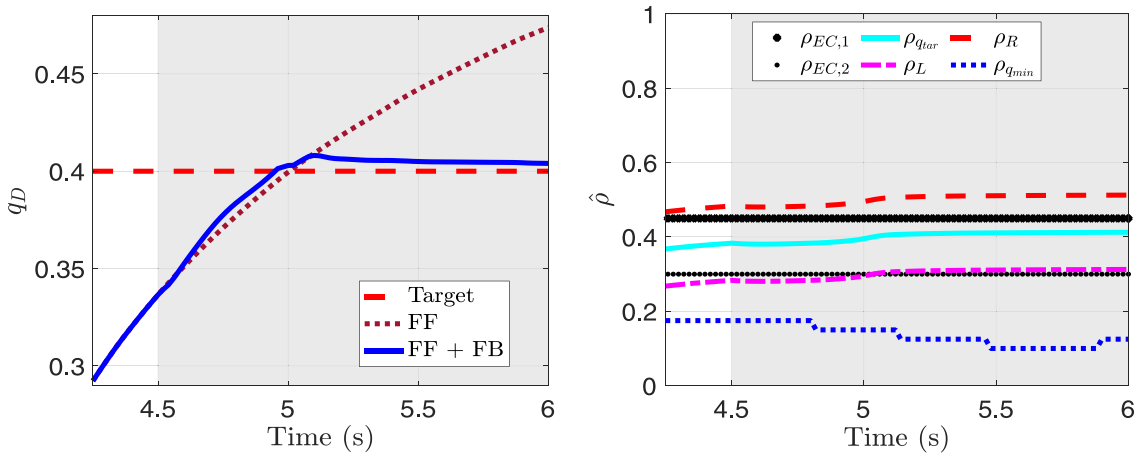

Fig. 3. Case 1 - fixed ECH&CD: q_D (left), ECCD position (right).

1. The first step involves defining the set Ω as follows. Suppose the EC position at time step t_k is $\boldsymbol{\rho}_{ec} := [\rho_{ec,1}, \ldots, \rho_{ec,n_{ec}}]^T$. Furthermore, suppose that $\bar{\delta}_j$ represents the maximum distance the jth EC position can change in a single time-step. Let $\Delta_j := \{\delta_{j,1} = -\bar{\delta}_j, \delta_{j,2}, \ldots, \delta_{j,n_{j,\delta_j}} = \bar{\delta}_j\}$ represent the discrete set of possible changes in the jth EC position, where n_{j,δ_j} the total number of possible numbers by which the value of $\rho_{ec,j}$ can be changed. Thus, the set $\Omega_j := \{\rho_{ec,j} + \delta_{j,1}, \ldots, \rho_{ec,j} + \delta_{j,n_{j,\delta_j}}\}$ represents the set of positions jth ECH&CD can take in the next time step. Then, the set Ω of possible ECH&CD positions is given by different combinations of the positions in the sets $\Omega_1, \ldots, \Omega_{n_{ec}}$, i.e., $\Omega := \Omega_1 \times \cdots \times \Omega_{n_{ec}}$.
2. The second step involves iterating through the vector of possible EC positions in the set Ω. For each vector of EC positions, the corresponding auxiliary powers are computed using (30). The cost corresponding to each EC position is computed and recorded using the cost function formula given in (26).
3. The optimal EC positions and auxiliary powers at time step t_k correspond to the one with the least cost function value.

A detailed algorithm for implementing the above iterative approach on a plasma control system (PCS) is given in Appendix E. The Appendix also discusses method to reduce the computational expense of the above approach.

4. Numerical simulations

The controller was tested using nonlinear simulations in the Control Oriented Transport SIMulator (COTSIM) for a DIII-D tokamak scenario. The simulator uses the 1D magnetic diffusion equation, the electron-heat-transport equation, and the semi-empirical Bohm/Gyro-Bohm model to simulate tokamak plasma dynamics [22]. Two different cases, fixed and moving ECH&CD, were considered in the simulations. This section presents and analyzes the simulation results. The DIII-D configuration information and input data were taken from the 147634 DIII-D shot in the simulations. In the simulations, 2 NBIs and 2 ECCDs were used for feedback control. The feedforward (FF) components of these inputs are presented in Figs. 4, 5, 7 and 8. The rational safety factor surface corresponding to $q = 1.5$ was considered for gradient control in both the simulation cases. Note that the safety factor value of $q = 1.5$ may sometimes be achieved at two different locations. For instance, consider the case where the minimum safety factor of the q-profile is equal to $1.5 - \epsilon$ for a given time instant, where ϵ is a small constant. Since the q-profile is continuous, the rational surface corresponding to $q = 1.5$ will be achieved at both sides of the safety factor minimum. If such cases appear in the simulations, the rational surface on the right of the safety factor minimum is considered for gradient control. The gradient was approximated using (11) with $h = 0.1$. The target is both the simulations was set as $q_D = 0.4$. In all the simulations, the controller was activated at $t = 4.5$ seconds. This choice of the controller activation time was selected based on two aspects. First, the q-profile must achieve the target safety factor value of $q = 1.5$ before the controller is activated. Second, recall that the gradient is approximated using the central difference given in (11). Such an approximation is valid when the safety factor is locally a straight line. Thus, the controller must be activated when this assumption is valid. The gray background in all the figures referred to in this section corresponds to the period when the controller is active.

4.1. Case 1: Fixed ECH&CD case

Fig. 3 shows the closed-loop system's evolution when both the ECH&CD are spatially fixed. For the fixed ECH&CD case, the auxiliary powers can be computed using (30) with $\boldsymbol{g}_D^* = \boldsymbol{g}_D(\bar{\boldsymbol{\rho}}_{ec})$ and $c_D^* = c_D(\bar{\boldsymbol{\rho}}_{ec})$ in (27) defined with respect to the fixed EC positions shown in Fig. 3. As evident from Fig. 3, the feedforward and the closed-loop trajectory of q_D follow a similar path during the first 0.5 s of the simulation. However, beyond $t = 5$ seconds, the closed-loop trajectory follows the target slope of $q_D = 0.4$ closely until the end of the simulation. The right subfigure in Fig. 3 shows the location of the rational surface $\bar{\rho}$, the location of the minimum safety factor ρ_{min}, the left and right control points ρ_L and ρ_R, respectively. The NBI and ECH&CD powers are given in Figs. 4 and 5, respectively. The figures show the saturation of the actuator powers during the initial phase of the simulation. In addition, the second ECH&CD's power $P_{ec,2}$ is also saturated for the bulk of the simulation.

4.2. Case 2: Moving ECH&CD case

The results from moving ECH&CD simulations are shown in Figs. 6, 7, and 8. At each time-step, both the ECH&CDs were assumed to move a maximum distance of $\hat{\rho} = 0.01$, i.e., $\bar{\delta}_1 = \bar{\delta}_2 = 0.01$. In addition, the sets Δ_1, Δ_2 comprised of nine equidistant points in between -0.01 and 0.01. The controller in the simulations implemented Algorithm 1 (given in Appendix E) to compute the optimal EC positions and auxiliary powers. The left subfigure of Fig. 6 illustrates that the controller achieves the desired target slope of $q_D = 0.4$ within 0.25 s of controller activation. The right subfigure displays the values of $\bar{\rho}$, ρ_{min}, ρ_L, and ρ_R. The subfigure also shows the EC positions $\rho_{ec,1}$, $\rho_{ec,2}$ at each time t. Even though the initial EC positions differ, both $\rho_{ec,1}$ and $\rho_{ec,2}$ eventually converge to an optimal global location as determined by the controller. It is important to note that the existence of a single global optimal EC position is not guaranteed in all scenarios. Figs. 7 and 8 show the NBI and ECH&CD powers, respectively. The powers saturate for an initial period and then

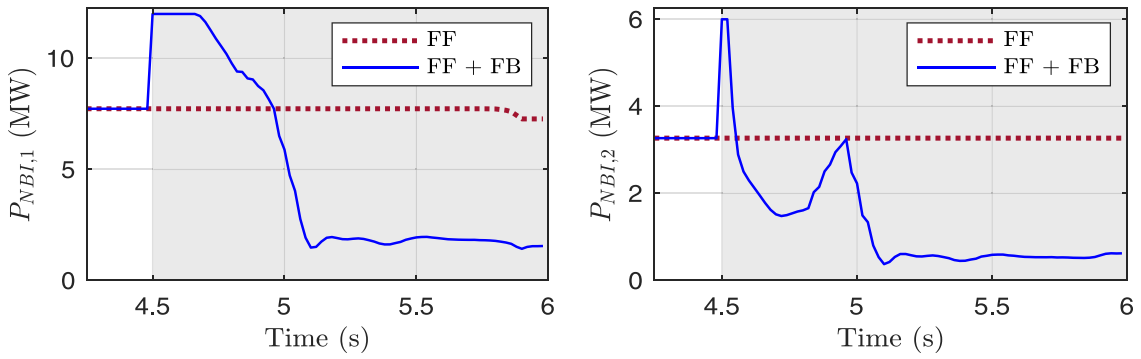

Fig. 4. Case 1 - fixed ECH&CD: Auxiliary powers - $P_{nb,1}$ (left), $P_{nb,2}$ (right).

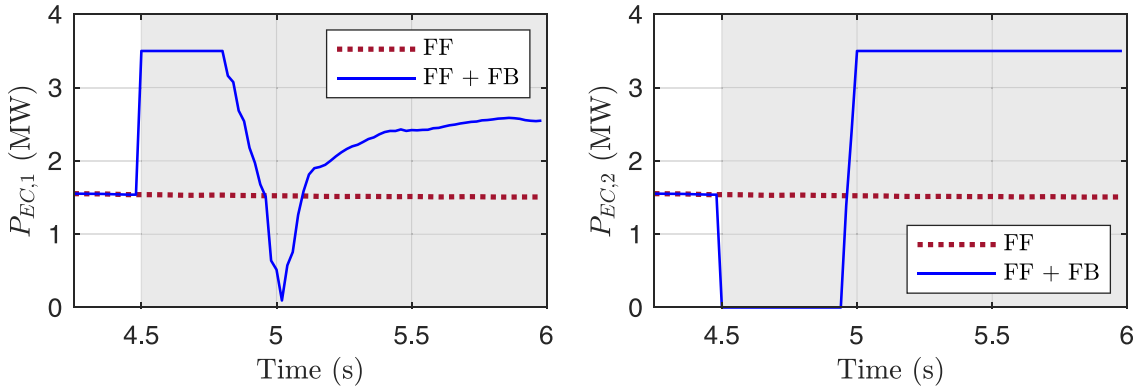

Fig. 5. Case 1 - fixed ECCD: Auxiliary powers - $P_{ec,1}$ (left), $P_{ec,2}$ (right).

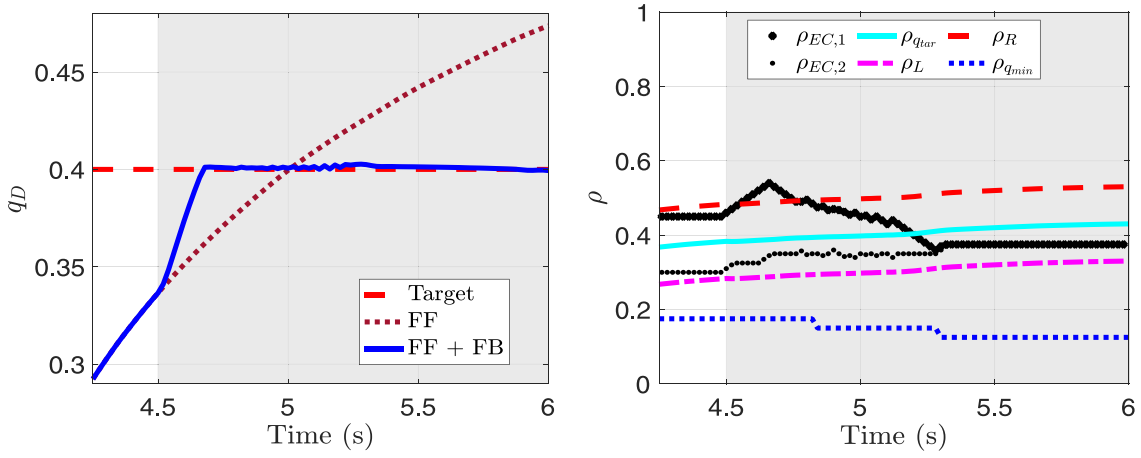

Fig. 6. Case 2 - moving ECH&CD: q_D (left), ECCD position (right).

go into high-frequency chatter-like behavior before achieving stable (no chatter) values. Note that the high-frequency behavior in the input powers corresponds to the transience in the EC positions $\rho_{ec,1}$ and $\rho_{ec,2}$ (shown in the right subfigure of Fig. 6). Thus, slight changes in the EC positions can significantly alter the optimal ECH&CD and NBI powers. After going through the chatter, the ECH&CD powers gradually increase while NBI powers decrease over time. Since the feedforward trajectory moves away from the target during this phase (evident from Fig. 6), the powers of ECH&CDs, which are positioned closer to the two gradient control points, gradually increase to track the target in the closed-loop (feedforward + feedback) case. Consequently, the NBI powers gradually decrease with time to satisfy the total power constraint (28).

4.3. Comparison of fixed and moving ECH&CD cases

A comparison of the two cases discussed above shows differences in the controller effectiveness and performance. First, even though the control objective is achieved in both cases, the target slope is achieved sooner in the moving ECH&CD case. Notably, the target is achieved in less than 0.25 s of controller activation in the moving ECH&CD case compared to 0.5 s in the fixed ECH&CD case. This difference in convergence time is significant because the controller is active only in a short time window (1.5 s) of the discharge. Furthermore, the closed-loop trajectory tracks the target more closely in the moving ECH&CD case. Another significant difference between the two cases can be observed in the auxiliary powers. The input powers in the moving ECH&CDcase exhibit a high-frequency behavior, which is absent in the

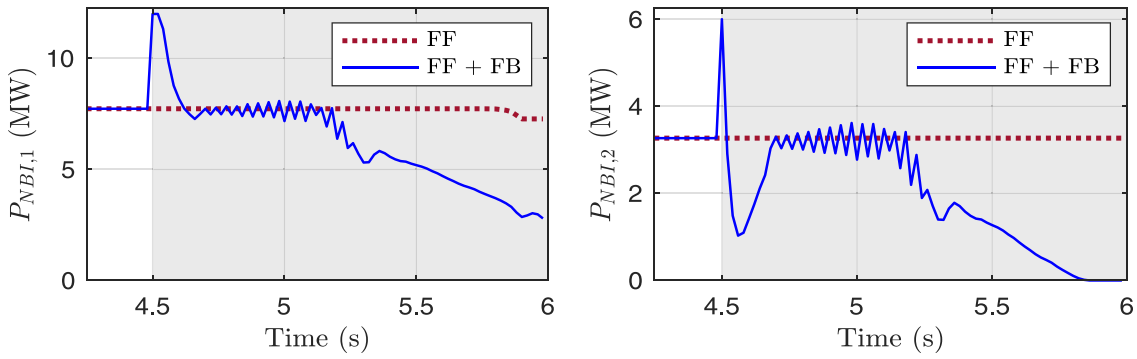

Fig. 7. Case 2 - moving ECH&CD: Auxiliary powers - $P_{nb,1}$ (left), $P_{nb,2}$ (right).

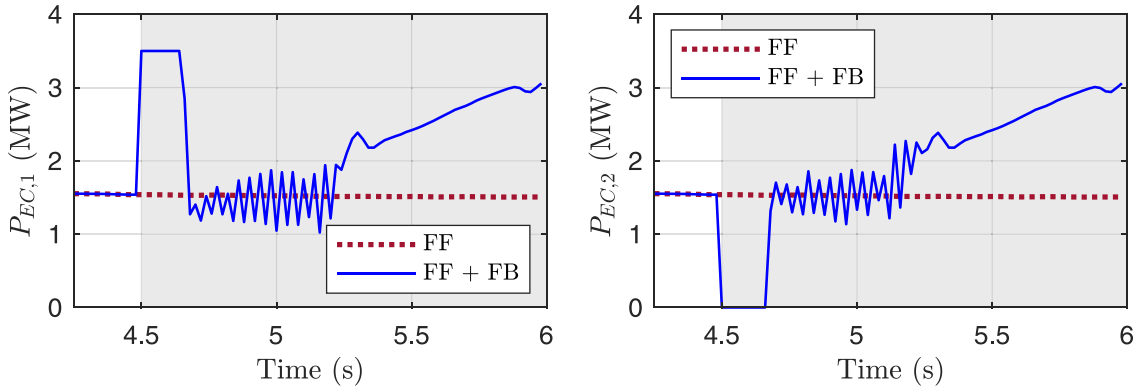

Fig. 8. Case 2 - moving ECH&CD: Auxiliary powers - $P_{ec,1}$ (left), $P_{ec,2}$ (right).

fixed case. On the other hand, the saturation observed in the second ECH&CD's power of the fixed case is not present in the moving case. Similar saturation was observed while controlling the minimum safety factor with fixed and moving ECH&CD [17].

5. Conclusion

A model-based local safety factor gradient control is presented. A nonlinear model that governs the evolution of the slope of the safety factor gradient at a spatially moving rational surface is first developed. The model incorporates the effect of ECH&CD position of the gradient dynamics, thus allowing it to be treated as a controllable variable. Then, a control algorithm based on optimal feedback linearization of the nonlinear model is developed to regulate the safety factor gradient around a given target. The control algorithm is designed to allocate noninductive powers and ECH&CD positions simultaneously. The control algorithm is tested for a DIII-D tokamak scenario using nonlinear simulations in the Control Oriented Transport SIMulator (COTSIM). Both fixed and moving ECH&CD cases are studied. The results demonstrate the effectiveness of the proposed and the advantage of implementing a moving ECH&CD for control. Future studies may include methods to eliminate chatter in the input power when the ECH&CD positions are updating and experimental validation of the proposed controller.

CRediT authorship contribution statement

Sai Tej Paruchuri: Conceptualization, Methodology, Investigation, Writing – original draft, Visualization, Validation. **Eugenio Schuster:** Conceptualization, Validation, Writing – review & editing, Supervision, Project administration, Funding acquisition.

Declaration of competing interest

The authors declare that they have no known competing financial interests or personal relationships that could have appeared to influence the work reported in this paper.

Data availability

No data was used for the research described in the article.

Acknowledgments

This material is based upon work supported by the U.S. Department of Energy, Office of Science, Office of Fusion Energy Sciences, under Award Numbers DE-SC0010661 and DE-SC0021385.

Disclaimer

This report was prepared as an account of work sponsored by an agency of the United States Government. Neither the United States Government nor any agency thereof, nor any of their employees, makes any warranty, express or implied, or assumes any legal liability or responsibility for the accuracy, completeness, or usefulness of any information, apparatus, product, or process disclosed, or represents that its use would not infringe privately owned rights. Reference herein to any specific commercial product, process, or service by trade name, trademark, manufacturer, or otherwise does not necessarily constitute or imply its endorsement, recommendation, or favoring by the United States Government or any agency thereof. The views and opinions of authors expressed herein do not necessarily state or reflect those of the United States Government or any agency thereof.

Appendix A. Magnetic diffusion equation

The magnetic diffusion equation (MDE) [23] is one dimensional partial differential equation that governs the evolution of the poloidal stream function ψ and takes the form

$$\frac{\partial \psi}{\partial t} = \frac{\eta}{\mu_0 \rho_b^2 \hat{F}^2} \frac{1}{\hat{\rho}} \frac{\partial}{\partial \hat{\rho}} \left(\hat{\rho} D_\psi \frac{\partial \psi}{\partial \hat{\rho}} \right) + R_0 \hat{H} \eta j_{ni} \tag{A.1}$$

subject to the boundary conditions

$$\left. \frac{\partial \psi}{\partial \hat{\rho}} \right|_{\hat{\rho}=0} = 0, \qquad \left. \frac{\partial \psi}{\partial \hat{\rho}} \right|_{\hat{\rho}=1} = - \underbrace{\frac{\mu_0}{2\pi} \frac{R_0}{\hat{G}_{\hat{\rho}=1} \hat{H}_{\hat{\rho}=1}}}_{k_{I_p}} I_p. \tag{A.2}$$

The terms η, μ_0, j_{ni} and I_p in the above equation are the plasma resistivity, vacuum permeability, noninductive current and plasma current, respectively. On the other hand, the terms $\hat{F}$, $\hat{G}$ and $\hat{H}$ are functions of the spatial variable $\hat{\rho}$ and define the magnetic configuration of the plasma equilibrium. The function D_ψ is computed using the formula $D_\psi = \hat{F}\hat{G}\hat{H}$. The plasma resistivity η is computed using the control-oriented model developed in [24], which is given by

$$\eta \approx g_\eta \times (I_p^\gamma P_{tot}^\epsilon \bar{n}_e^\zeta)^{-3/2}, \tag{A.3}$$

where the terms P_{tot}, $\bar{n}_e$ and g_η are the total power, line-average electron density and fixed function of the spatial variable $\hat{\rho}$ respectively. The terms γ, ϵ and ζ in the above equation are the scaling constants. The noninductive current in (A.1) is approximated using the control-oriented model

$$\begin{aligned} \eta j_{ni} \approx & \sum_{i=1}^{n_{nb}} g_{nb,i} \times (I_p^\gamma P_{tot}^\epsilon \bar{n}_e^\zeta)^{(-3/2+\epsilon_{nb})} \bar{n}_e^{-1} P_{nb,i} \\ & + \sum_{j=1}^{n_{ec}} \bar{g}_{ec,j} \times (I_p^\gamma P_{tot}^\epsilon \bar{n}_e^\zeta)^{(-3/2+\epsilon_{ec})} \bar{n}_e^{-1} P_{ec,j} \\ & + (\partial \psi / \partial \hat{\rho})^{-1} g_{bs} \times (I_p^\gamma P_{tot}^\epsilon \bar{n}_e^\zeta)^{-1/2} \bar{n}_e. \end{aligned} \tag{A.4}$$

The above model was first introduced in [24]. By formulation, it assumes that there are n_{nb} NBIs and n_{ec} ECH&CDs available for local gradient control. In the above model, the terms $g_{nb,i}$ $(i = 1, \ldots, n_{nb})$, $\bar{g}_{ec,j}$ $(j = 1, \ldots, n_{ec})$, g_{bs} are functions of $\hat{\rho}$ that account for the NBI, ECH&CD and bootstrap current depositions, respectively. The scalars ϵ_{nb} and ϵ_{ec} are constants that account for NBI and ECH&CD efficiency, respectively. The terms $P_{nb,i}$, $P_{ec,j}$ are the powers corresponding to the ith NBI and jth ECH&CD, respectively. In this work, these powers are the primary controllable inputs. On the other hand, the terms I_p, $\bar{n}_e$ and P_{tot} are considered the prescribed inputs. Typically, there are other controllers running in parallel to the local gradient controller which prescribe these values. For example, the total energy controller prescribes the values of P_{tot} to track a target total energy [14]. However, detailed discussion of these controllers is beyond the scope of the current work, and the parameters are treated as known inputs in the simulations conducted for this study. Note that the total power P_{tot} can be expressed in terms of NBI and ECH&CD powers as

$$P_{tot} = \sum_{i=1}^{n_{nb}} P_{nb,i} + \sum_{j=1}^{n_{ec}} P_{ec,j}. \tag{A.5}$$

Since the value of P_{tot} is prescribed, the local gradient controller must satisfy the above equation while allocating the NBI and ECH&CD powers.

Substituting (A.3), (A.4) into (A.1) and taking the derivative with respect to the spatial derivative results in a PDE of the form

$$\begin{aligned} \dot{\theta} = & \left(h_{\eta,1} \theta'' + h_{\eta,2} \theta' + h_{\eta,3} \theta \right) u_\eta + \sum_{i=1}^{n_{nb}} h_{nb,i} u_{nb,i} \\ & + \sum_{j=1}^{n_{ec,j}} \bar{h}_{ec,j} u_{ec,j} + \left(h_{bs,1} \frac{1}{\theta} - h_{bs,2} \frac{\theta'}{\theta^2} \right) u_{bs}, \end{aligned} \tag{A.6}$$

subject to the boundary conditions

$$\theta(0) = 0, \qquad \theta(1) = -k_{I_p} I_p, \tag{A.7}$$

where

$$\begin{aligned} h_{\eta,1} &:= \frac{1}{\mu_0 \rho_b^2} \frac{g_\eta}{\hat{F}^2} D_\psi, \\ h_{\eta,2} &:= \frac{1}{\mu_0 \rho_b^2} \left[\left(\frac{g_\eta}{\hat{F}^2} \right)' D_\psi + \frac{g_\eta}{\hat{F}^2} \left(\frac{D_\psi}{\hat{\rho}} + 2 D_\psi' \right) \right], \\ h_{\eta,3} &:= \frac{1}{\mu_0 \rho_b^2} \left[\left(\frac{g_\eta}{\hat{F}^2} \right)' \left(\frac{D_\psi}{\hat{\rho}} + D_\psi' \right) + \frac{g_\eta}{\hat{F}^2} \left(\frac{D_\psi' \hat{\rho} - D_\psi}{\hat{\rho}^2} \right) \right], \\ h_{nb,i} &:= R_0 \times (\hat{H} \times g_{nb,i})', \\ \bar{h}_{ec,j} &:= R_0 \times (\hat{H} \times \bar{g}_{ec,j})', \\ h_{bs,1} &:= R_0 \times (\hat{H} \times g_{bs})', \\ h_{bs,2} &:= R_0 \times \hat{H} \times g_{bs}, \\ u_\eta &:= (I_p^\gamma P_{tot}^\epsilon \bar{n}_e^\zeta)^{-3/2}, \\ u_{nb,i} &:= (I_p^\gamma P_{tot}^\epsilon \bar{n}_e^\zeta)^{(-3/2+\zeta_{nb})} \bar{n}_e^{-1} P_{nb,i}, \\ u_{ec,j} &:= (I_p^\gamma P_{tot}^\epsilon \bar{n}_e^\zeta)^{(-3/2+\zeta_{ec})} \bar{n}_e^{-1} P_{ec,j}, \\ u_{bs} &:= (I_p^\gamma P_{tot}^\epsilon \bar{n}_e^\zeta)^{-1/2} \bar{n}_e. \end{aligned} \tag{A.8}$$

Recall that the term θ in the above PDE is the poloidal flux gradient, which is defined as $\theta := \frac{\partial \psi}{\partial \hat{\rho}}$. The terms u_η, $u_{nb,i}$, $u_{ec,j}$ and u_{bs} in (A.6) are the virtual inputs terms. The notations $\dot{(\cdot)}$ and $(\cdot)'$ represent the derivatives with respect to the temporal t and spatial $\hat{\rho}$ variables, respectively. Since the time derivative of q depends on $\dot{\theta}$ (refer to (3)), the above PDE is crucial in deriving the final model necessary for local gradient control design. However, prior to proceeding to final model development, it is important to incorporate the effect of ECH&CD positions on the θ dynamics. The next section focuses on addressing this aspect of modeling.

Appendix B. Modeling the relation between ECH&CD position and safety factor dynamics

The poloidal flux gradient model derived in the previous section does not incorporate the effect of EC positions on the plasma dynamics. In particular, the model assumes that the EC positions are fixed, say at $\bar{\rho} := [\bar{\rho}_{ec,1}, \ldots, \bar{\rho}_{ec,n_{ec}}]^T$. Shifting the jth ECH&CD's position from $\bar{\rho}_{ec,j}$ to $\rho_{ec,j}$ shifts the corresponding current deposition profile. Suppose that the current deposition profile corresponding to the jth ECH&CD positioned at $\bar{\rho}_{ec,j}$ is $\bar{\jmath}_{ec,j}^{prof} : \hat{\rho} \mapsto \bar{\jmath}_{ec,j}^{prof}(\hat{\rho})$. If the EC position shifts from $\bar{\rho}_{ec,j}$ to $\rho_{ec,j}$, then the new current deposition profile can be mathematically expressed as

$$\jmath_{ec,j}^{prof}(\rho_{ec,j}, \hat{\rho}) := \bar{\jmath}_{ec,j}^{prof}(\hat{\rho} + \bar{\rho}_{ec,j} - \rho_{ec,j}). \tag{B.1}$$

The current deposition profile appears in (A.6) through $\bar{h}_{ec,j}$ (defined in (A.8)). The term $\bar{g}_{ec,j}$ in (A.8) is related to the current deposition profile [14,24] as

$$\bar{g}_{ec,j}(\hat{\rho}) = \bar{\jmath}_{ec,j}^{prof}(\hat{\rho}) \frac{(T_e^{prof}(\hat{\rho})(n_e^{prof}(\hat{\rho}))^\zeta)^{\lambda_{ec}}}{n_e^{prof}(\hat{\rho})}, \tag{B.2}$$

where T_e^{prof} and n_e^{prof} are fixed functions of the spatial variable $\hat{\rho}$, ζ and λ_{ec} are constants. The effect of jth EC position on the plasma dynamics is modeled by using $\jmath_{ec,j}^{prof}$ instead of $\bar{\jmath}_{ec,j}^{prof}$ in (B.1) and replacing $\bar{h}_{ec}$ in (A.6) by h_{ec}, which is defined as

$$h_{ec,j}(\rho_{ec,j}, \hat{\rho}) := R_0 (\hat{H}(\hat{\rho}) g_{ec,j}(\rho_{ec,j}, \hat{\rho}))' \tag{B.3}$$

with

$$g_{ec,j}(\rho_{ec,j}, \hat{\rho}) := \jmath_{ec,j}^{prof}(\rho_{ec,j}, \hat{\rho}) \frac{(T_e^{prof}(\hat{\rho})(n_e^{prof}(\hat{\rho}))^\zeta)^{\lambda_{ec}}}{n_e^{prof}(\hat{\rho})}. \tag{B.4}$$

Thus, the new governing equation for the evolution of the poloidal flux gradient is

$$\dot{\theta} = \left(h_{\eta,1}\theta'' + h_{\eta,2}\theta' + h_{\eta,3}\theta\right)u_\eta + \sum_{i=1}^{n_{nb}} h_{nb,i}u_{nb,i} + \sum_{j=1}^{n_{ec}} h_{ec,j}(\rho_{ec,j},\cdot)u_{ec} + \left(h_{bs,1}\frac{1}{\theta} - h_{bs,2}\frac{\theta'}{\theta^2}\right)u_{bs}. \tag{B.5}$$

The above PDE is subject to the same boundary conditions as the PDE in (A.6).

Appendix C. Stability analysis of controller

The goal of this section is to determine if the controller drives the error gradient $\tilde{q}_D := q_D - \bar{q}_D$ to 0 eventually. The stability analysis is carried out using the standard Lyapunov stability theorem [20] and the closed-loop system's equation (derived in Section 3.1).

$$\dot{\tilde{q}}_D = -k_p\tilde{q}_D - k_I\int_0^t \tilde{q}_D. \tag{C.1}$$

The theorem states that if there exists a positive definite function of the form $V : x \to V(x)$, where x is the state of a nonlinear system governed by an ODE of the form $\dot{x} = f(x)$, such that its time-derivative $\dot{V}$ is negative definite, then the equilibrium of the closed-loop system is asymptotically stable, i.e., $\tilde{q}_D \to 0$ as $t \to \infty$ [20].

To perform the stability analysis on the system of interest, consider the positive definite Lyapunov function

$$V = \frac{1}{2}x^T\underbrace{\begin{bmatrix}1 & b\\ b & k_I\end{bmatrix}}_{P}x \tag{C.2}$$

with $x = [x_1, x_2]^T := [\tilde{q}_D, \int_{t_0}^t \tilde{q}_D dt]^T$, and the constant b satisfying $0 < b < \min(\sqrt{k_I}, k_P k_I/(k_I + \frac{1}{4}k_P^2))$. Note that since the constant b satisfies the condition $0 < b < \sqrt{k_I}$, the matrix P has positive eigenvalues, which in turn implies that the Lyapunov function is positive definite, i.e., $V(x) \geq 0$ for all x and $V = 0$ if and only if $x = 0$. Taking the time derivative of the Lyapunov function results in the equation

$$\dot{V} = -(K_P - b)x_1^2 - K_I b x_2^2 - K_p b x_1 x_2. \tag{C.3}$$

The time derivative satisfies the condition $\dot{V}(x) \leq 0$ for all x and $\dot{V} = 0$ if and only if $x = 0$. Thus, the time derivative $\dot{V}$ is negative definite. The stability theorem stated above gives us the required conclusion that $\tilde{q}_D \to 0$ as $t \to \infty$. In fact the theorem implies that the integral of the gradient error $\int_{t_0}^t \tilde{q}_D dt$ also converges to 0, which is a stronger conclusion.

Appendix D. Optimization analysis

Lagrange multiplier analysis is one of the most commonly used methods for solving an optimization problem. Suppose that the optimization problem considers the minimization of a cost function (say f) with respect to parameters (say $\boldsymbol{u}_{fb}$) subject to the linear constraints $g_1^*(\boldsymbol{u}_{fb}) = 0$ and $g_2(\boldsymbol{u}_{fb}) = 0$. The Lagrange multiplier analysis starts with considering the Lagrangian function $\mathcal{L}$, which is defined as

$$\mathcal{L}(\boldsymbol{u}_{fb}, \lambda_1, \lambda_2) = f(\boldsymbol{u}_{fb}) - \lambda_1 g_1^*(\boldsymbol{u}_{fb}) - \lambda_2 g_2(\boldsymbol{u}_{fb}). \tag{D.1}$$

According to the Lagrange multiplier theorem [25], if an extremum exists $\boldsymbol{u}_{fb}$, then there are Lagrange multipliers λ_1^*, λ_2^* such that

$$\nabla\mathcal{L}(\boldsymbol{u}_{fb}^*, \lambda_1^*, \lambda_2^*) = 0, \tag{D.2}$$

which is equivalent to

$$\nabla f - \lambda_1^*\nabla g_1^* - \lambda_2^*\nabla g_2 = 0, \tag{D.3}$$

$$g_1^* = 0, \tag{D.4}$$

$$g_2 = 0. \tag{D.5}$$

For the problem at hand, the cost function f and the constraints g_1^* and g_2 are defined as in (26), (29) and (28), respectively. Using these definitions, and applying the first condition given above results in

$$2Q\boldsymbol{u}_{fb} - \lambda_1^*\boldsymbol{g}_D^* - \lambda_2^*\mathbf{1} = 0, \tag{D.6}$$

which implies

$$\boldsymbol{u}_{fb}^* = \frac{1}{2}Q^{-1}\left(\lambda_1^*\boldsymbol{g}_D^* + \lambda_2^*\mathbf{1}\right). \tag{D.7}$$

Substituting the expression for $\boldsymbol{u}_{fb}$ into the constraint equations gives us

$$\underbrace{\begin{bmatrix}\boldsymbol{g}_D^{*T}Q^{-1}\boldsymbol{g}_D^* & \boldsymbol{g}_D^{*T}Q^{-1}\mathbf{1}\\ \mathbf{1}Q^{-1}\boldsymbol{g}_D^* & \mathbf{1}Q^{-1}\mathbf{1}\end{bmatrix}}_{A}\begin{Bmatrix}\lambda_1^*\\ \lambda_2^*\end{Bmatrix} = \underbrace{\begin{bmatrix}-2c_D^*\\ -2c_p\end{bmatrix}}_{c}. \tag{D.8}$$

Thus, the optimal feedback inputs $\boldsymbol{u}_{fb}^*$ can be computed from (D.7) as

$$\boldsymbol{u}_{fb}^* = \frac{1}{2}Q^{-1}\begin{bmatrix}\boldsymbol{g}_D^* & \mathbf{1}\end{bmatrix}A^{-1}\boldsymbol{c}. \tag{D.9}$$

The above extremum is indeed a minimum for the problem at hand. Since f defined in (26) is quadratic, the cost function value of $f(\boldsymbol{u}_{fb}^*)$ is the least possible achievable value such that $g_1^*(\boldsymbol{u}_{fb}^*) = 0$ and $g_2(\boldsymbol{u}_{fb}^*) = 0$.

Appendix E. Algorithm

This section presents the algorithm for computing the optimal combination of auxiliary drive powers and EC positions at any given time-step. These values are optimal in the sense that they are the solutions of the discrete-time version of the optimization problem formulated in Section 3.2. In the algorithm, the subscript/superscript k refers to the kth time-step.

Algorithm 1: Algorithm for optimization problem with moving ECCD.

Inputs: $\boldsymbol{\rho}_{ec}^{k-1} = [\rho_{ec,1}^{k-1}, \ldots, \rho_{ec,n_{ec}}^{k-1}]^T$, $\bar{\delta}_1, \ldots, \bar{\delta}_{n_{ec}}$.

Outputs: $\boldsymbol{u}_{fb}^{*,k}$, $\boldsymbol{\rho}_{ec}^{*,k}$.

1. Define the sets $\Omega_1, \ldots, \Omega_{n_{ec}}$ as given in Section 3.2.2, Step 1.
2. Define the set of possible EC positions as $\Omega := \Omega_1 \times \ldots \times \Omega_{n_{ec}}$.
3. For $i = 1, \ldots, n_{1,\delta_1} \times \ldots \times n_{n_{ec},\delta_{n_{ec}}}$ (number of elements in Ω),
   (a) Choose i^{th} element of Ω and set it as $\boldsymbol{\rho}_{ec,i}^k$.
   (b) Compute optimal auxiliary powers $\boldsymbol{u}_{fb,i}^{*,k}$ with $\boldsymbol{g}_D^* := \boldsymbol{g}_D(\boldsymbol{\rho}_{ec,i}^k)$ and $c_D^*(t) := c_D(\boldsymbol{\rho}_{ec,i}^k)$ using (30). Set $J_i^k = \boldsymbol{u}_{fb,i}^{*,k\,T}Q\boldsymbol{u}_{fb,i}^{*,k}$.
4. Set j such that $J_j^k = min_i J_i^k$. Set $u^{*,k} = u_j^{*,k}$ and $\boldsymbol{\rho}_{ec}^{*,k} = \boldsymbol{\rho}_{ec,j}^k$.

The above algorithm requires the implementation of mathematical operations such as numerical differentiation (to compute RHS of (B.3)) and matrix inversion/solving linear systems (to solve the RHS of (30)). However, implementing algorithms to carry out these mathematical operations in the PCS is straightforward.

Note that elements in sets are unordered by definition. However, in the above algorithm, it is assumed that each element in the set Ω is indexed, which allows us to iterate through the set sequentially.

Elements of Ω can be arbitrarily indexed since the final optimal solution is independent of indexing.

The computational expense of the above presented approach depends on the number of times (30) is used to compute the number of auxiliary powers. This is equal to the number of elements in the set Ω, which has $n_{1,\delta_1} \times \cdots \times n_{n_{ec},\delta_{n_{ec}}}$ elements. The computational expense of the above algorithm can be reduced by using the following methods.

1. The computation of each iteration is independent of other iterations. Thus, parallel computing or loop vectorization can be used to decrease the total computational time.
2. Multiple ECH&CDs can be combined into different clusters to decrease the number of elements in the set Ω.
3. Considering a coarser set of positions in the set Ω_j for the jth EC position reduces the number of iterations in the above presented algorithm.

References

[1] J.E. Barton, K. Besseghir, J. Lister, E. Schuster, Physics-based control-oriented modeling and robust feedback control of the plasma safety factor profile and stored energy dynamics in ITER, Plasma Phys. Control. Fusion 57 (11) (2015) 115003, http://dx.doi.org/10.1088/0741-3335/57/11/115003.

[2] M.D. Boyer, J. Barton, E. Schuster, T.C. Luce, J.R. Ferron, M.L. Walker, D.A. Humphreys, B.G. Penaflor, R.D. Johnson, First-principles-driven model-based current profile control for the DIII-D tokamak via LQI optimal control, Plasma Phys. Control. Fusion 55 (10) (2013) 105007, http://dx.doi.org/10.1088/0741-3335/55/10/105007.

[3] C. Xu, Y. Ou, E. Schuster, Sequential linear quadratic control of bilinear parabolic PDEs based on POD model reduction, Automatica 47 (2) (2011) 418–426, http://dx.doi.org/10.1016/j.automatica.2010.11.001.

[4] Y. Ou, C. Xu, E. Schuster, J. Ferron, T. Luce, M. Walker, D. Humphreys, Receding-horizon optimal control of the current profile evolution during the ramp-up phase of a tokamak discharge, Control Eng. Pract. 19 (1) (2011) 22–31, http://dx.doi.org/10.1016/j.conengprac.2010.08.006.

[5] E. Maljaars, F. Felici, M. de Baar, J. van Dongen, G. Hogeweij, P. Geelen, M. Steinbuch, Control of the tokamak safety factor profile with time-varying constraints using MPC, Nucl. Fusion 55 (2) (2015) 023001, http://dx.doi.org/10.1088/0029-5515/55/2/023001.

[6] E. Maljaars, F. Felici, T. Blanken, C. Galperti, O. Sauter, M. de Baar, F. Carpanese, T. Goodman, D. Kim, S. Kim, M. Kong, B. Mavkov, A. Merle, J. Moret, R. Nouailletas, M. Scheffer, A. Teplukhina, N. Vu, Profile control simulations and experiments on TCV: A controller test environment and results using a model-based predictive controller, Nucl. Fusion 57 (12) (2017) 126063, http://dx.doi.org/10.1088/1741-4326/aa8c48.

[7] F.B. Argomedo, E. Witrant, C. Prieur, S. Brémond, R. Nouailletas, J.-F. Artaud, Lyapunov-based distributed control of the safety-factor profile in a tokamak plasma, Nucl. Fusion 53 (3) (2013) 033005, http://dx.doi.org/10.1088/0029-5515/53/3/033005.

[8] F.B. Argomedo, C. Prieur, E. Witrant, S. Bremond, A Strict Control Lyapunov Function for a Diffusion Equation With Time-Varying Distributed Coefficients, IEEE Trans. Automat. Control 58 (2) (2013) 290–303, http://dx.doi.org/10.1109/TAC.2012.2209260.

[9] B. Mavkov, E. Witrant, C. Prieur, E. Maljaars, F. Felici, O. Sauter, Experimental validation of a Lyapunov-based controller for the plasma safety factor and plasma pressure in the TCV tokamak, Nucl. Fusion 58 (5) (2018) 056011, http://dx.doi.org/10.1088/1741-4326/aab16a.

[10] N.T. Vu, R. Nouailletas, E. Maljaars, F. Felici, O. Sauter, Plasma internal profile control using IDA-PBC: Application to TCV, Fusion Eng. Des. 123 (2017) 624–627, http://dx.doi.org/10.1016/j.fusengdes.2017.02.074.

[11] M. Boyer, J. Barton, E. Schuster, M. Walker, T. Luce, J. Ferron, B. Penaflor, R. Johnson, D. Humphreys, Backstepping Control of the Toroidal Plasma Current Profile in the DIII-D Tokamak, IEEE Trans. Control Syst. Technol. 22 (5) (2014) 1725–1739, http://dx.doi.org/10.1109/TCST.2013.2296493.

[12] J. Barton, M. Boyer, W. Shi, W. Wehner, E. Schuster, J. Ferron, M. Walker, D. Humphreys, T. Luce, F. Turco, B. Penaflor, R. Johnson, Physics-model-based nonlinear actuator trajectory optimization and safety factor profile feedback control for advanced scenario development in DIII-D, Nucl. Fusion 55 (9) (2015) 093005, http://dx.doi.org/10.1088/0029-5515/55/9/093005.

[13] A. Pajares, E. Schuster, Safety factor profile control in tokamaks via feedback linearization, in: 2016 IEEE 55th Conference on Decision and Control (CDC), 2016, pp. 5668–5673, http://dx.doi.org/10.1109/CDC.2016.7799140, Journal Abbreviation: 2016 IEEE 55th Conference on Decision and Control (CDC).

[14] A. Pajares, E. Schuster, Current profile and normalized beta control via feedback linearization and Lyapunov techniques, Nucl. Fusion (2021) 21.

[15] M. Boyer, R. Andre, D. Gates, S. Gerhardt, I. Goumiri, J. Menard, Central safety factor and β_N control on NSTX-U via beam power and plasma boundary shape modification, using TRANSP for closed loop simulations, Nucl. Fusion 55 (5) (2015) 053033, http://dx.doi.org/10.1088/0029-5515/55/5/053033.

[16] A. Pajares, E. Schuster, Robust nonlinear control of the minimum safety factor in tokamaks, in: 2021 IEEE Conference on Control Technology and Applications, CCTA, 2021, pp. 753–758, http://dx.doi.org/10.1109/CCTA48906.2021.9659126.

[17] S.T. Paruchuri, A. Pajares, E. Schuster, Minimum safety factor control in tokamaks via optimal allocation of spatially moving electron cyclotron current drive, in: 2021 60th IEEE Conference on Decision and Control, CDC, 2021, pp. 454–459, http://dx.doi.org/10.1109/CDC45484.2021.9683130.

[18] J. Ferron, M. Walker, L. Lao, H.S. John, D. Humphreys, J. Leuer, Real time equilibrium reconstruction for tokamak discharge control, Nucl. Fusion 38 (7) (1998) 1055–1066, http://dx.doi.org/10.1088/0029-5515/38/7/308.

[19] J.-J.E. Slotine, W. Li, Applied Nonlinear Control, Prentice Hall Englewood Cliffs, NJ, 1991.

[20] H.K. Khalil, Nonlinear Systems, 3rd Edition, Pearson, 2001.

[21] O.L. Mangasarian, Nonlinear Programming, SIAM, 1994.

[22] A. Pajares, Integrated Control in Tokamaks using Nonlinear Robust Techniques and Actuator Sharing Strategies (Ph.D. thesis), Lehigh University, Bethlehem, PA, USA, 2019.

[23] F.L. Hinton, R.D. Hazeltine, Theory of plasma transport in toroidal confinement systems, Rev. Modern Phys. 48 (2) (1976) 239–308, http://dx.doi.org/10.1103/RevModPhys.48.239.

[24] J.E. Barton, W. Shi, K. Besseghir, J. Lister, A. Kritz, E. Schuster, T.C. Luce, M.L. Walker, D.A. Humphreys, J.R. Ferron, Physics-based control-oriented modeling of the safety factor profile dynamics in high performance tokamak plasmas, in: 52nd IEEE Conference on Decision and Control, 2013, pp. 4182–4187, http://dx.doi.org/10.1109/CDC.2013.6760531.

[25] M.R. Hestenes, Optimization Theory: The Finite Dimensional Case, 1st Edition, Krieger Pub Co, New York, 1975.